Modeling and experimentation of a passive low frequency nanoforce sensor based on diamagnetic levitation.

Joël Abadie, Emmanuel Piat, Stéphane Oster, Mehdi Boukallel

Modeling and experimentation of a passive low frequency nanoforce sensor based on diamagnetic levitation

J. Abadie[a,*], E. Piat[a], S. Oster[a], M. Boukallel[b]

[a] *Femto-st Institute, UMR CNRS 6174, UFC - ENSMM - UTBM, France*
[b] *CEA List, Laboratoire des Interfaces Sensorielles et Ambiantes, 18 route du Panorama, Fontenay aux Roses, France*

Abstract

This paper is focused on the study of a new low frequency micro and nanoforce sensor based on diamagnetic levitation. The force sensitive part is a ten-centimeter long macroscopic capillary tube used as a levitating seismic mass. This tube presents a naturally stable equilibrium state with six degrees of freedom thanks to the combination of diamagnetic repulsive and magnetic attractive forces. It is only used as a one-direction force sensing device along its longitudinal axis. This force sensor is passive. The force measurement is based on the displacement of the capillary tube and in steady-state this displacement is proportional to the force. This sensor is characterized by an under-damped second-order linear force-displacement dynamic which remains linear on several hundred micrometers and can thus measure a wide range of microforces. Because of the magnetic springs configuration used, the capillary tube presents a horizontal mechanical stiffness that can be adjusted between 0.01 and 0.03 N/m (similar to the stiffness of a thin AFM cantilever). The measurement range typically varies between ± 50 μN. Bandwidth is 4 Hz. The resolution depends on the sensor used to measure the capillary tube displacement and on noises induced by environmental conditions (ground and air vibrations). The resolution typically reached with a STIL confocal chromatic sensor is 5 nN inside a test

*Corresponding author
Email address: jabadie@femto-st.fr (J. Abadie)

chamber located on a anti-vibration table. This study is illustrated by a pull-off force measurement.
Keywords: micro and nano force sensor, magnetic spring, diamagnetism

---

1. Introduction

Because force effects can be measured in many different ways, micro and nanoforce sensor designs are numerous. The majority is based on monolithic elastic microstructures which are most of the time microcantilevers [1] coupled or not with a mechanical deformation amplifier : AFM based microforce sensors using two or four quadrants photodetectors [2] [3] or the interferometry principle [4], piezoresistive microforce sensors which use the variation of the piezoresistive layer resistance when a force is applied [5] [6], capacitive microforce sensors which make use of change in capacitance between two metal plates when their distance changes during force application [7] [8], piezoelectric microforce sensors which generate a voltage when they are stressed by a force [9], etc. Because maximum microstructure deformations are usually small, these sensors are mostly limited in range of force measurement but have a large frequency bandwidth. A few sensors can exhibit larger deformations or displacements. For instance, the maximum deformation of the nanoforce sensor presented in [10] is several dozen micrometers thanks to a special elastic mechanical design with a very small stiffness. Unlike accelerometers which use seismic mass principle to measure acceleration, microforce sensors based on a rigid seismic mass like in this article are really uncommon. A force sensor with a range measurement of several millinewtons and based on a mass moving inside a pneumatic linear bearing is described in [11]. The mass is 21.17 grammes and the force resolution is 0.5 micronewton. The air friction inside the bearing is assumed small enough to be neglected.

The force measurement field is an emergent market with a potentially large growth and some micro and nano force sensors are already commercially available. Companies producing nanomaterial and micromechanical devices, firms using micro encapsulation, research laboratories in the field of micro and nano technologies and finally the more restricted market of biomedical research are potential users of force sensors. There are very few industrial actors on this market excepted AFM manufacturers. One can list for instance *Picotwist* which

is an innovative high-tech company that has recently brought a fully-featured, plug-and-play version of the magnetic trap apparatus for single-molecule manipulation onto market [12]. *Tetra GmbH* company proposes a microforce measurement system for microtribology applications [13] [14]. *CSM Instrument* company[1] has brought a nanotribometer and a nanoindenter using microforce sensors onto market. *Femtotools*[2] has designed a capacitive microforce sensor for high resolution measurements with a large bandwidth (7.8 kHz) [8]. Finally, Robomat [15] was an important project funded in 2005 with a partnership between *Conti Temic GmbH* (Nürnberg, Deutschland), *Forschungszentrum Caesar* (Bonn, Deutschland), *Amic GmbH* (Berlin, Deutschland), *Klocke Nanotechnik* (Aachen, Deutschland) and *Nanoscale Technologies GmbH* (Kassel, Deutschland). The aim of this project is the development of a microrobot-based measurement and test system for indentation and scratch tests, with an integrated imaging system for microtopography.

To conclude this short review, contrary to micro force sensors based on microcantilevers, micro and nano force-sensor studies based on a macroscopic seismic mass seems little developed and the use of diamagnetic levitation to design such a sensor remains an original approach.

All micro and nanoforce-sensor designs are constrained by the fact that only force effects can be directly measured. Because of this, a force sensitive part is needed in order to observe these effects which can be either the deformation of an elastic microstructure or the displacement of a rigid seismic mass. Appropriate sensors are used to measure the signal related to the deformation or displacement x of the sensitive part. The usual scalar expression used to calculate the component F of the applied force $\vec{F}$ in one direction $\vec{x}$ of space is thus:

[1] http://www.csm-instruments.com
[2] http://www.femtotools.com

$$F = K\,x \qquad K > 0 \tag{1}$$

where K is the mechanical stiffness of the sensitive part along $\vec{x}$ (by convention x is set to zero when there is no deformation or displacement). Equation (1) does not take into account the transient dynamic response of the sensitive part excited by the force.

The new micro/nanoforce sensor design proposed is based on a seismic mass which is a rigid levitating tube made of glass that will be called *maglevtube*. This tube levitates passively and is stabilized around a given equilibrium state thanks to repulsive diamagnetic effects coupled with attractive magnetic effects. Because the *maglevtube* can move with 6 degrees of freedom (three rotations and three translations) around its equilibrium configuration, the combination of diamagnetic and magnetic effects forms what will be called a *magnetic spring* with an associated stiffness K for each dof of the maglevtube like in the equation (1). The maglevtube has a microscopic tip where the external force to be measured is applied. The sensor is currently designed to only measure forces applied along the longitudinal axis $\vec{x}$ of the tube. It can be classified as a sensor based on macroscopic seismic mass. Very few microforce sensors are based on this principle. Almost all the realization, in this field, are based on elastic microstructures (see table 1). The main avantage of the levitation sensor (LEV) is the use of standard equipment for its fabrication. Microstructures need heavy equipment like a clean room, photolithography, DRIE, etc. As the seismic mass can be easily measured with a precision balance, the calibration of the LEV can be performed using a simple procedure. Nevertheless the magnetic levitation associated with macroscopic weight induces a small bandwidth. Such a sensor is well designed for measurement of quasi-static forces. The levitation sensor characteristics compared to the other realizations are summarized in table 1.

This paper deals with the design and the modeling of the described force sen-

sor. Experimentation is also provided. First of all, the diamagnetic levitation principle will be developed to introduce the concept of passive magnetic springs. Secondly, the experimental prototype will be presented. The dynamic modeling and the simulation of the 3 dimensional non-linear behaviours will be described. Nevertheless, the calculation based on quaternions will only be briefly described. Thirdly, the linearity of the sensor along $\vec{x}$ direction will be characterized and a linear model will be proposed. The calibration process (identification of the linear dynamic model) will be described and finally an experimental measurement example will be given.

	Seismic mass (Macro)	**Elastic Structure (Micro)**
Deformation or displacement amplitude	High: 2 mm (LEV)	Low: several dozen of micrometers [16]
Resolution	High: 10 nN (LEV)	High: • Capacitive force sensor: 19.9 nN [17] • Strain gauge sensor: 2 nN [18]
Structure stiffness	Low: 0.01 N/m (LEV)	Medium: typically 0.1 N/m to 100 N/m for AFM cantilevers
Bandwidth	Low: 4 Hz (LEV)	High: *Femtotools* 7.8 kHz [8]
Deformation or displacement measurement	Outsourced by optical sensor: • Confocal chromatic sensor (LEV) • Optical interferometer [11]	Outsourced: optical sensor for AFM [2] [3] Internalized (micro fabricated): • Strain gauge [19] • Capacitive force sensor [20] • Piezo-electric sensor [21] dimensional developed
Ease of fabrication	Easy by conventional means (LEV)	Heavy equipment (μ-fabrication, cleanroom): • AFM cantilever [1] • Complex multi DOF microstructures [22] [21] [23]
Calibration	Simplified (LEV)	Complex approaches: AFM cantilever calibration [24]

Table 1: Levitation sensor compared to other force sensors.

2. Diamagnetic levitation and micro force measurement

The two basic approaches to achieve magnetic levitation are either passive or active. The term active is used for systems using a feedback control loop, in opposite to systems levitating passively which do not require any control. In active magnetic levitation configurations, sensors for monitoring the position of the suspended object are needed (in general, one sensor per controlled DOF). Because displacement sensors are difficult to integrate in microdevices, passive levitation is particularly interesting is this context.

Passive levitation is commonly unstable. This result was shown theoretically for the electrostatic case by Earnshaw in 1841 [25] and for both electrostatic and magnetic cases by Braunbek [26]. According to the Earnshaw theorem, stable free suspension of a permanent magnet in the magnetic field of another magnet is not possible. He proved that a configuration consisting in bodies which attract or repel one another with a force proportional to the inverse square of the distance between them is unstable. The most complete theory of the possibility and the conditions for a free levitation are given by Boerdijik [26]. He proved that free levitation in constant magnetic field is possible only with the use of materials with a relative permeability μ_r inferior to 1 such as diamagnetic materials. This is mainly due to the magnetic response of diamagnetic materials to an external magnetic field. When the external magnetic field is applied to a diamagnetic material, the latter becomes magnetized in the opposite direction of the applied magnetic field. For this reason, a force is produced which causes the diamagnetic material to be expelled from the magnetic field.

2.1. Stable configuration allowing free levitation of permanent magnets

There are three basic diamagnetic bearing configurations allowing stable free levitation of permanent magnets [27]. Each of them is represented in figure 1. In the first configuration on the left, it is possible to stabilize the equilibrium

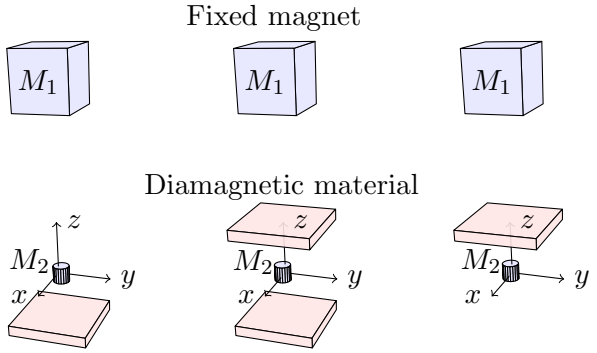

Figure 1: Basic configurations used to achieve stable passive levitation of a permanent magnet M_2.

state of the small magnet M_2 by placing a diamagnetic material closely below it. The latter exercises an upward force of repulsion upon M_2 which increases if M_2 comes closer to the diamagnetic material. If the vertical distance between the magnet M_1 and the diamagnetic material is correctly chosen (this distance depends on the mass of M_2, the magnetization of M_1 and M_2 and on the susceptibility of the diamagnetic material), any slight lowering of M_2 from the equilibrium state results in an increase in the repulsion exercised by the diamagnetic body and a decrease of the attraction force between the two magnets M_1 and M_2. The sum of both is always superior to the weight of M_2, thus M_2 moves up and returns to its equilibrium position [27]. If a slight upward displacement of M_2 from the equilibrium state is made, the magnetic attractive force is more important, but the diamagnetic repulsion decreases. The sum of both is always lower than the weight of M_2 thus M_2 moves down. In the two remaining configurations, the diamagnetic levitation works in a similar way.

2.2. Diamagnetic suspension mechanism

The suspension mechanism L adopted is a variation of the three configurations previously presented (see figure 2). Two identical (material, geometry,...) magnets M_1 and M_1' are used with north and south poles in opposite direction on the vertical axis. The levitating magnet M_2 is placed between the two fixed

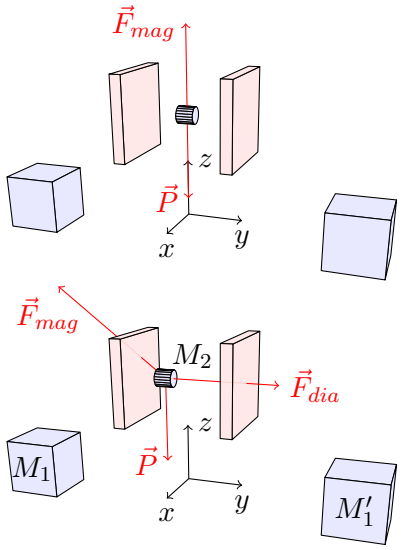

Figure 2: Suspension mechanism L

magnets such that the attractive forces $\vec{F}_{mag}$ compensates the weight of M_2. The resulting equilibrium state is stable in the plan $(\vec{x}, \vec{z})$ but unstable along $\vec{y}$ because any slight displacement of M_2 along $\vec{y}$ will increase the y component of the magnetic forces $\vec{F}_{mag}$ and M_2 will move towards M_1 or M_1'. This unstable equilibrium is stabilized with the addition of two diamagnetic plates. It can be shown that $\vec{F}_{dia}$ components along $\vec{x}$ and $\vec{z}$ are negligible (as they are extremely small compared to the component along $\vec{y}$) thus the diamagnetic forces $\vec{F}_{dia}$ can be considered to be only along axis $\vec{y}$ [28]. In this case $\vec{F}_{dia}$ is always opposed to the magnetic attraction along $\vec{y}$ and will compensate any displacement along $\vec{y}$. The expression of $\vec{F}_{mag}$ is given by [27]:

$$\vec{F}_{mag} = \vec{m} \iiint_{v_m} \nabla \vec{B} dv \tag{2}$$

where $\vec{m}$ is the permanent magnetization of the magnet M_2 (supposed constant inside M_2) and $\vec{B}$ the magnetic field created by the M_1 and M_1' magnets at the center of an elementary volume dv of M_2. The term v_m is the total volume of

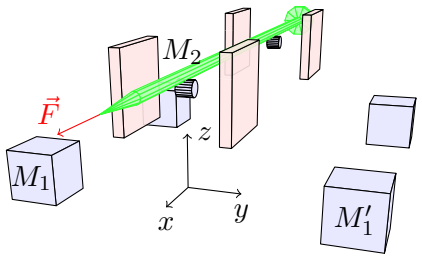

Figure 3: Principle of the levitating force sensing device.

M_2. The diamagnetic force is given by [27]:

$$\vec{F}_{dia} = \frac{\chi_m}{\mu_0} \iiint_{v_g} \vec{B}_T . \nabla \vec{B}_T \, dv \tag{3}$$

where χ_m is the susceptibility of the diamagnetic material, μ_0 the absolute permeability of free space, and $\vec{B}_T$ the magnetic field created by all the magnets M_1 and M_2 at the center of an elementary volume dv of the diamagnetic material. The term v_g is the total volume of the diamagnetic material.

Figure 3 shows the principle of the levitating force sensing device. It uses two suspension mechanisms $L1$ and $L2$ spaced out in order to reduce the influence between each other. The two levitating magnets M_2 are jointed by a thin capillary glass tube to make up the maglevtube. The first end of the maglevtube is sharpened and constitutes the sensing area. the other end is equipped with a plane deflector used to facilitate the measurements of the x displacement of the tube. The maglevtube is considered as a seismic mass mechanically connected to a virtual magnetic spring. The levitating part is only used as a one direction force sensing device. The force $\vec{F}$ to be measured is assumed to be colinear with $\vec{x}$ and has the following components in the global reference frame given in figure 3:

$$\vec{F} \begin{bmatrix} F^x \\ 0 \\ 0 \end{bmatrix} \tag{4}$$

	Material	Magnetic property	Dimension
Magnet M_1	NdFeB	B_r= 1.3 T	10 mm x 10 mm x 10 mm
Magnet M_2	NdFeB	B_r=0.95 T	ϕ 1.6 mm x 2.3 mm
Capillary tube	Glass	-	ϕ 0.45 mm x 95 mm
Sharpened extremity	Glass	-	ϕ 0.02 mm x 1 mm
Diamagnetic material	Graphite	$\chi_m = -12 \times 10^{-5}$	30 mm x 20 mm x 3 mm

Table 2: Force sensor components.

3. Experimental prototype

Table 2 presents the characteristic of each element that has been used for the experimental prototype. The mass m of the maglevtube is 74 mg and its length is 9.5 cm. The diamagnetic material used is a pyrolytic graphite with a diamagnetic susceptibility χ_m equal to -12×10^{-5}. The air gap between the two graphite plates is 2 mm. Figure 4 is a top view of the experimental prototype. A zoom shows the maglevtube tip in contact with an AFM cantilever. The x displacement of the maglevtube is measured by a CL2 confocal chromatic sensor manufactured by STIL SA which is fixed and targeted at the deflector stuck at the rear of the maglevtube. The confocal sensor only measures the distance l between the deflector and the CL2 head. If the maglevtube remains oriented along $\vec{x}$ the measurement of l is representative of the position x of the maglevtube (see section 4.1). The position of the four magnets M_1 is independently adjustable along the $\vec{y}$ direction. Thus, it is possible to vary the stiffness of the

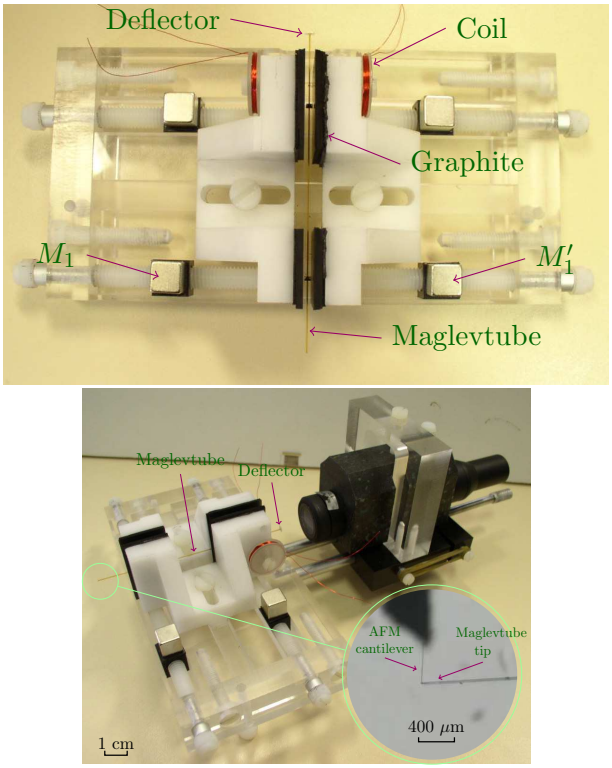

Figure 4: Force sensor prototype.

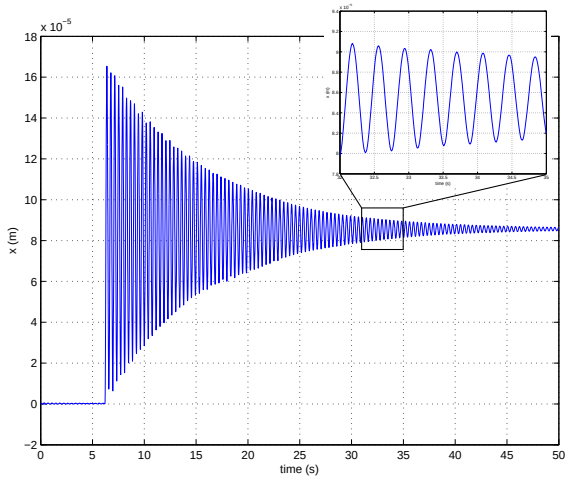

Figure 5: Experimental response of the maglevtube to a 0.1 A current step.

magnetic springs presented in section 2.2. Having different distances between M_1 and M_1' for suspension mechanisms $L1$ and $L2$, also makes an adjustment of the horizontal attitude of the maglevtube possible.

The two coils added to the rear of the sensor on either side of the two rear diamagnetic plates (deflector side) are used during the calibration process (see section 6). They are designed to apply an external force on the maglevtube along $\vec{x}$. When the coils are supplied with a current i, they modify the local magnetic field around the rear magnet of the maglevtube. This creates an external electromagnetic force that generates a displacement along $\vec{x}$. Figure 5 shows the under-damped and long time dynamic response of the maglevtube after a current step of 0.1 A applied at $t = 6.2$ s into the coils. As this response is similar to a second-order transfer function, an approximation of the stiffness K can be deduced from this curve after the measurement of the mass m of the maglevtube and the frequency f of the signal pulsation:

$$K \cong 4\pi^2 f^2 m \tag{5}$$

The value of K is around 0.02 N/m. In order to improve the analysis of the dynamic behaviour of the maglevtube a complete 3D dynamic modeling is presented in the next section.

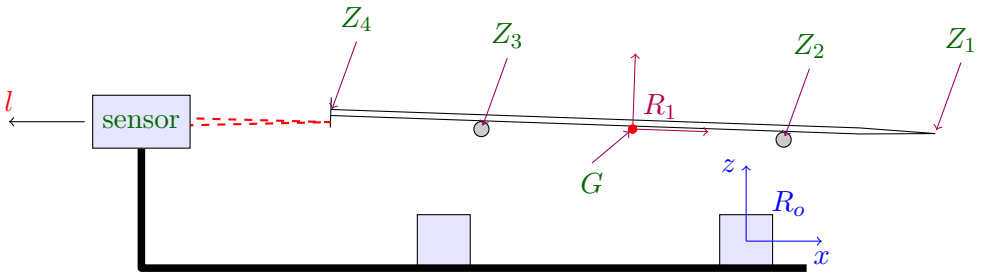

Figure 6: 3D modeling of the sensor.

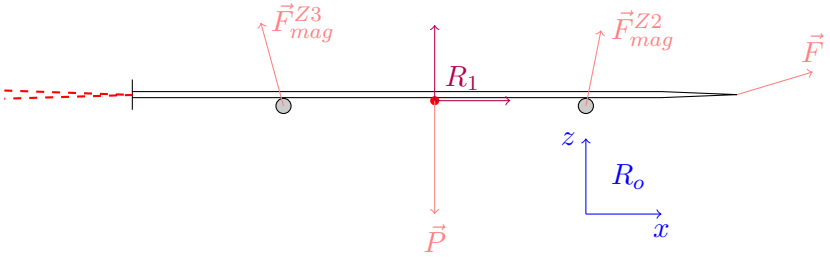

Figure 7: forces applied on the maglevtube.

4. Three dof non linear dynamic modeling

All of the six degrees of freedom of the maglevtube can be excited and exhibit particular trajectories. Understanding these trajectories requires investigation of the system behavior using dynamic modeling. The maglevtube is considered as a rigid body of mass m with a centre of gravity G and having a moment of inertia tensor $\bar{I}$. A local reference frame R_1, attached on G, is used to express the geometry of the maglevtube in a local way (see figure 6). The points corresponding to the sensitive area (Z_1), the localization of the levitating magnets (Z_2,Z_3) and the deflector (Z_4) are expressed in R_1, where their coordinates remain constant. The Newton law is used to calculate the dynamic trajectory of G:

$$\sum \vec{F}_{ext} = m\,\vec{\ddot{G}} \qquad \text{with} \quad \vec{\ddot{G}} = \left| \begin{array}{c} \ddot{x}_G \\ \ddot{y}_G \\ \ddot{z}_G \end{array} \right|_{R_0} \tag{6}$$

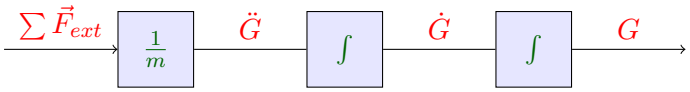

Figure 8: Numerical resolution of the maglevtube position.

$\vec{F}_{ext}$ represents the different forces applied to the mass m (see figure 7). They are the external force $\vec{F}$ applied on the sensitive area, the magnetic forces $F_{mag}^{Z_2}$ $F_{mag}^{Z_3}$ and the diamagnetic forces $F_{dia}^{Z_2}$ $F_{dia}^{Z_3}$ applied to the magnets M_2, the friction force F_{visc} due to the drag of the surrounding air and the weight $\vec{P}$. $\ddot{\vec{G}}$ is the acceleration of the mass written in the Galilean reference frame R_0. To completely describe the mass trajectory, it is also necessary to take into account its rotation in 3D space. Because levitation is similar to the behavior of spacecrafts, the representation of the attitude of the maglevtube has been inspired by [29]. It uses the formalism of quaternions. The rotation dynamic behavior written in the reference frame R_1 is given by the equation:

$$\sum \vec{M}_{F/_G} = \bar{I}\,\dot{\vec{\Omega}} + \vec{\Omega} \wedge (\bar{I}\,\vec{\Omega}) \qquad \text{with} \quad \dot{\vec{\Omega}} = \left| \begin{array}{c} \dot{p} \\ \dot{q} \\ \dot{r} \end{array} \right|_{R_1} \tag{7}$$

where $\vec{M}_{F/_G}$ are the different moments around G of the forces applied to the mass. The weight $\vec{P}$ is the only force that does not generate a torque that makes changes in the maglevtube attitude (see figure 7). $\vec{\Omega}$ is the instantaneous angular velocity vector written in the reference frame R_1. The components of $\vec{\Omega}$ are p, q and r in R_1.

4.1. Numerical resolution of the dynamic equations

A numerical resolution of the equations of the rigid body movement has been developed. The forces applied at each instant produce movement variations. In this way, the equation (6) can be easily solved to produce the trajectory of G (see figure 8). For the equation (7) which describes the rotational behaviour, the process is more complex. This equation is necessary to determine the angular velocity $\vec{\Omega}$ according to the different torques applied to the body. To determine

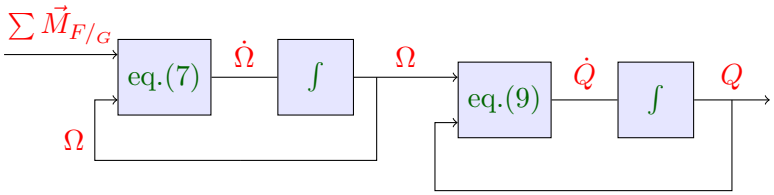

Figure 9: Numerical resolution of the maglevtube attitude.

the attitude of the maglevtube a quaternion Q has been used. Q characterizes the attitude, that is the orientation of the reference frame R_1 in R_0 (it is also the attitude of the maglevtube in R_0). The quaternion Q is equal to:

$$Q = q_0 + q_1\, i + q_2\, j + q_3\, k \tag{8}$$

where q_0, q_1, q_2 and q_3 are its components and i, j, k the quaternion's basis elements.

The variation of the attitude Q of the maglevtube, depends on the angular velocity $\vec{\Omega}$ according to:

$$\dot{Q} = \dot{q}_0 + \dot{q}_1\, i + \dot{q}_2\, j + \dot{q}_3\, k = \frac{1}{2} \begin{bmatrix} -p\, q_1 - q\, q_2 - r\, q_3 + \dots \\ (p\, q_0 - q\, q_3 + r\, q_2)\, i + \dots \\ (p\, q_3 + q\, q_0 - r\, q_1)\, j + \dots \\ (-p\, q_2 + q\, q_1 + r\, q_0)\, k \end{bmatrix} \tag{9}$$

where p, q and r are the components of $\vec{\Omega}$ calculated with equation (7) (see figure 9). A basic term to term integration of $\dot{Q}$ provides the components q_0, q_1, q_2, q_3 and thus the orientation of reference frame R_1 in R_0.

Figure 9 summarizes the different steps used to calculate the attitude Q of the maglevtube. This processing has been implemented as an input-output Matlab/Simulink block in which the end-user can apply external forces as inputs on different selected points on the maglevtube. The output is the distance l measured by the displacement sensor. The latter is aimed at the deflector in

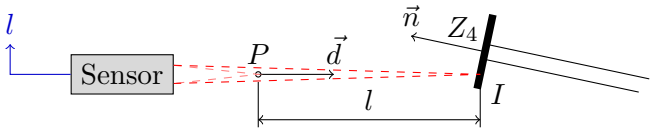

Figure 10: displacement measurement of the maglevtube.

the direction $\vec{d}$ (see figure 10). In practice $\vec{d}$ is colinear to $\vec{x}$. The distance l is given by:

$$l = \frac{\vec{n} \cdot P\vec{Z}_4}{\vec{n} \cdot \vec{d}} \qquad \text{with } \vec{PI} = l \cdot \vec{d} \tag{10}$$

where $\vec{n}$ is a normal vector defining the orientation of the deflector which is fixed on the maglevtube at Z_4. When the maglevtube is in its equilibrium configuration (with no external force), the deflector is on the point P and the measured distance l is set to zero. To calculate l at a given moment, it is necessary to use the position and the attitude of the maglevtube, because the components of $\vec{n}$ and Z_4 are initially defined in the reference frame R_1 (they are fixed points and fixed directions of the rigid body). Changing these components from R_1 to R_0 is done by using a transformation matrix that depends on the components of G and Q.

4.2. 3D simulator operation

The 3D simulator is programmed in C++ and implemented in a Matlab/Simulink s-function. This s-function calculates all the internal forces (magnetic, diamagnetic, weight, viscous friction of the air) applied to the maglevtube and solves (thanks to Simulink internal solver which makes the discretization of the time) its dynamic behaviour according to the equations provided in sections 2 and 4. It also provides an OpenGL rendering in which the different kind of forces and torques are visualized. The simplest usage consists in applying as input a force $\vec{F}$ to the sensitive area Z_4 (areas Z_1, Z_2 and Z_3 are also possible) and eventually a current i in the two coils mounted on the sensor (see figure 11). These coils generate an additional force applied to the maglevtube

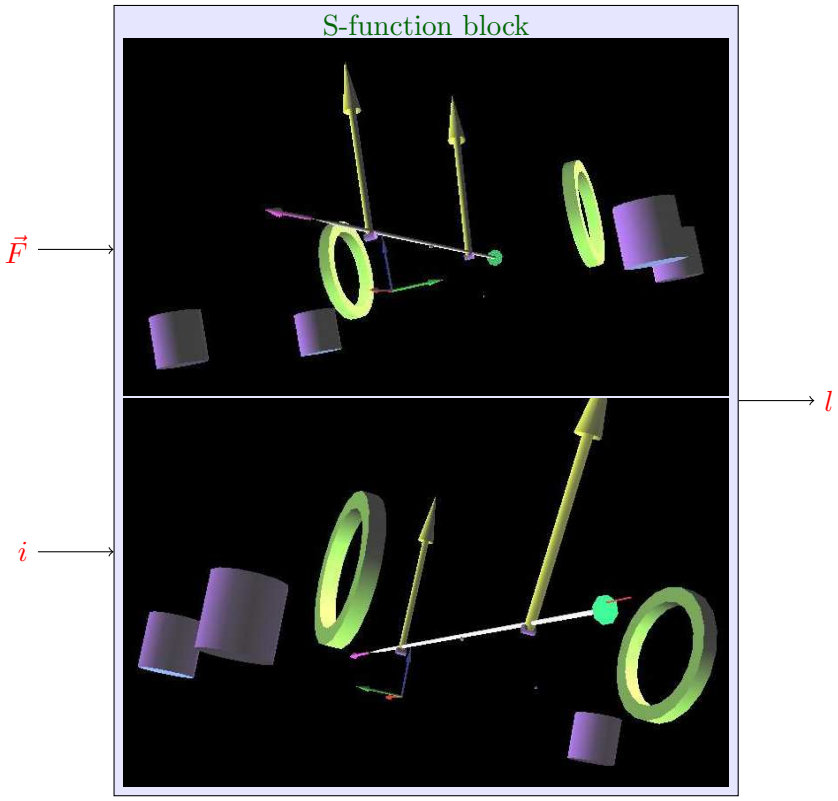

Figure 11: Simulink s-function block including 3D modeling and OpenGL rendering.

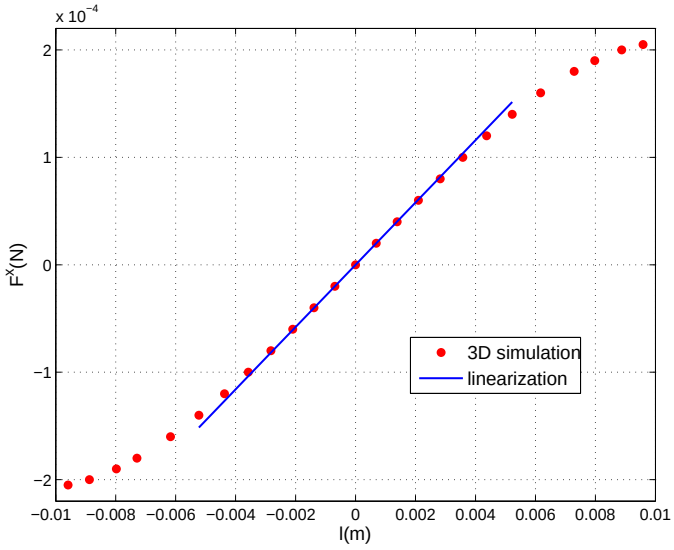

Figure 12: Force/displacement characteristic in the $\vec{x}$ direction.

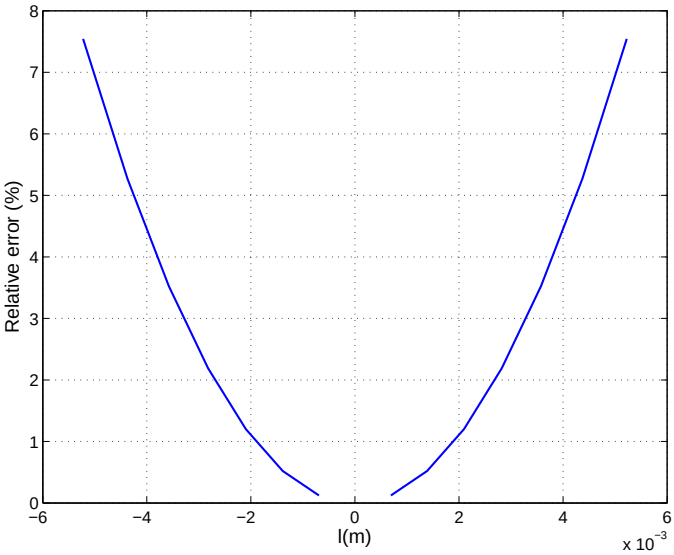

Figure 13: Relative error estimation between 3D model and linearization.

along the measurement direction $\vec{x}$ in R_0. The Matlab/Simulink workspace environment enables output data like the measurement l or the complete dynamic state of the maglevtube to be monitored. It is also possible to plot the magnetic force/torque fields. Vibrations can be communicated to the main magnets M_1 and the distance between them can be adjusted. Mechanical characteristics of the different maglevtubes used in the simulation can be modified.

This simulator has been used to determine the static characteristic of the sensor. An input force $\vec{F}$ is applied in the horizontal direction $\vec{x}$ (see equation (4)). The input-output transfer considered is the stationary transfer between F^x and the measured distance l when steady-state is reached. The force-displacement characteristic of this transfer is given in figure 12. The slope of this curve is the stiffness K of the sensor. Figure 13 shows the relative error ϵ between the linearized force F_{lin} and the non linear model:

$$\epsilon = \frac{F_{lin} - F^x}{F_{lin}} \times 100 \tag{11}$$

With displacements l between zero and 1.5 mm the sensor has a maximum relative error ϵ equal to 0.63 %. For greater displacements the magnetic sustentation mechanism generates important perturbations not only to the height of levitation z_G in R_0 but it also generates a parasite rotation of the maglevtube around the $\vec{y}$ direction. For displacements greater than 9.5 mm the passive levitation is broken.

5. Simplified one DOF linear dynamic modeling

To simplify the model of the sensor we have assumed that the external force $\vec{F}$ is applied along $\vec{x}$ (thus $\vec{F} = F^x\,\vec{x}$ according to equation (4)) and that the displacement l is lower than ± 1.5 mm. In this case a one dof simplified model is established by a projection of the differential vector equation (6) on $\vec{x}$:

$$F^x + F^x_{mag} + F^x_{visc} = m\,\ddot{x} \tag{12}$$

Let S be the fixed point corresponding to the position of G when the maglevtube is in steady-state without excitation ($\vec{F} = 0$). In case of small displacements around S (inferior to 1.5 mm max), the magnetic force F^x_{mag} is assumed linear (see section 4):

$$F^x_{mag} = -K^x_m\,x \tag{13}$$

where K^x_m is the magnetic stiffness and x is the fist component of $\vec{SG}$ in R_0. For small speeds, the viscous friction force is also assumed linear, thus:

$$F^x_{visc} = -K^x_{visc}\,\dot{x} \tag{14}$$

where K^x_{visc} is the viscous friction coefficient. According to equations (13) and (14), equation (12) becomes:

$$F^x - K^x_m\,x - K^x_{visc}\,\dot{x} = m\,\ddot{x} \tag{15}$$

5.1. Single input-single output model

The input of this system is the external force F^x applied along $\vec{x}$ to the tip on Z_1. The output is the tip position x (see figure 6). Thus the associated second-order transfer in Laplace domain is classically:

$$x(s) = G(s)\,F^x(s) \tag{16}$$

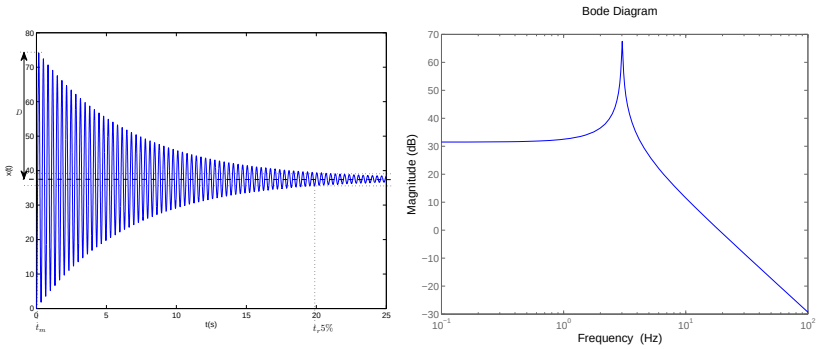

Figure 14: temporal unit step response ($F^x = 1$ N) and frequency response of the linear model.

$$G(s) = \frac{\frac{1}{m}}{s^2 + \frac{K^x_{visc}}{m} s + \frac{K^x_m}{m}} = \frac{k\,\omega_n^2}{s^2 + 2\,\xi\,\omega_n\,s + \omega_n^2} \tag{17}$$

with k the static gain, ξ the damping ratio and ω_n the undamped natural frequency:

$$k = G(0) = \frac{1}{K^x_m} \qquad \omega_n = \sqrt{\frac{K^x_m}{m}} \qquad \xi = \frac{K^x_m}{2\,m\,\omega_n} \tag{18}$$

The identification of the parameters performed on the experimental prototype gives (see section 6) $K^x_m = 0.026$ N/m, $K^x_{visc} = 2.2{\times}10^{-5}$ N.s/m, $m = 7.4{\times}10^{-5}$ kg, thus:

$$G(s) = \frac{13513}{s^2 + 0.3\,s + 360} \tag{19}$$

We find $k = 37.52$ m/N, $\xi = 7.9 \times 10^{-3}$ and $\omega_n = 18.98$ rad/s. The system has two complex conjugate poles p_1 and p_2 whose values are characteristic of an extreme oscillating behaviour and a long response time:

$$p_{1,2} = -\xi\,\omega_n \pm j\,\omega_n\sqrt{1-\xi^2} = -0.15 \pm 18.97\,j \tag{20}$$

Figure 14 shows the system response for a hypothetical unit step force F^x and the frequency response. The cutoff frequency at 3dB is $f_c = 4.7$ Hz. The temporal response is characterized by the following parameters related to the

system natural frequency ω_n and the damping ratio ξ:

Overshoot: $D\% = 100\, e^{-\frac{\pi\xi}{\sqrt{1-\xi^2}}} = 97.5\%$

Rise time: $t_m = \frac{1}{\omega_n\sqrt{1-\xi^2}(\pi - cos^{-1}\xi)} = 0.02s$

Settling time at 5%: $t_r = \frac{1}{\omega_n\xi} ln(\frac{100}{5\sqrt{1-\xi^2}}) = 19.9s$

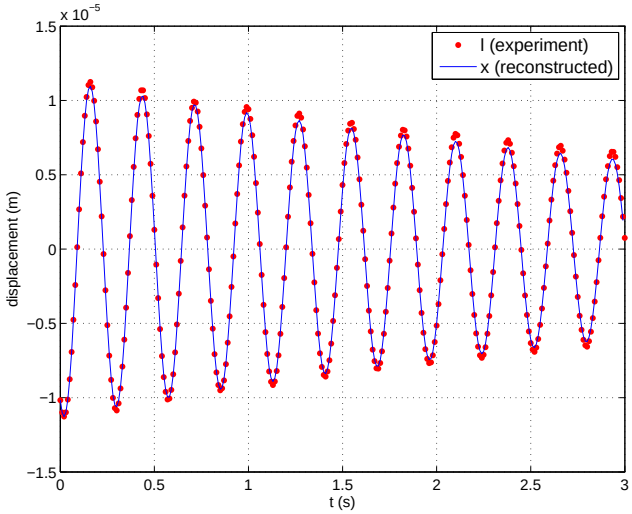

Figure 15: Measured and reconstructed zero input response (ZIR) of the maglevtube displacement.

6. Sensor calibration along $\vec{x}$

Calibration is a complex problem for micro and nanoforce sensors because of the lack of standard forces at this scale [11]: no international measurement institute supports a direct force realization linked to the International System of Units (SI) below 1 N, even for a constant force. Thus, calibration must be performed using indirect stationary or dynamic approaches and care must be taken with stiffness calculation. The characterization of measurement uncertainty for actual micro and nanoforce sensors is an open problem upon which international metrology laboratories are working [30]. At the present time, without any standard micro or nanoforces available, it is difficult to validate any force sensor calibration and the associated uncertainty. Most of the time, the uncertainty associated with calibrations is not provided in experiments requiring micro or nanoforce measurements (for instance the nanotribology field with AFM) because there is no way to validate it. Calibration remains an open problem in the scientific community which is using or designing such sensors [4]. One of the questions which arises is about the fact that even if a calibration seems cor-

rectly done, it will be illustrated that micro and nanoforce measurements cannot be guaranteed in all circumstances with actual sensors designs. For instance, AFM used in nanotribology is based on two separate calibrations: one for the normal force measurement and one for the lateral force. The first one necessitates characterizing the vertical bending of the cantilever. The second, which is much more difficult to achieve (and still problematic), necessitates the characterisation of its torsion. During friction, because of coupling effects, torsion will produce variations of the bending stiffness. Thus the normal force measurement accuracy is not guaranteed in these conditions. The same reasoning is valid for the lateral force measurement. The cantilever displacement (bending and torsion) is measured using the deviation on a four-quadrant photodetector of a laser spot reflected by the back side of the cantilever. The shape of the cantilever under complex loading has also an unknown influence on the laser spot position on the back side of the cantilever. These points and others not developed here result in significant force measurement errors. These errors can only be estimated with computing simulation in order to calculate the cantilever shape on which simulated known forces are applied [31]. The problem here is to develop realistic simulators of the force sensors in order to predict and analyze the measurement errors.

Several dynamic calibration methods have been investigated for force sensors specifically using a seismic mass. These methods are based on particular external force generation like impact force [32, 33], step force [34] and oscillating force [35, 36, 37, 38]. The calibration approach presented here is different: it only requires an unknown excitation force component F^x with the following dynamic:

$$\begin{cases} F^x(t) \neq 0 & t_0 \leq t < t_1 \quad \forall\, F^x \text{ (unknown force)}, \\ 0 & t \geq t_1. \end{cases} \tag{21}$$

The output l after t_1 is the zero input response (ZIR) of the maglevtube. The calibration of the sensor is achieved thanks to a parameters identification of (17)

with the ZIR under unknown initial conditions at t_1 (position and speed of the maglevtube at t_1). Thus, $F^x(t)$ temporal shape before t_1 doesn't matter. This identification process gives the stiffness K_m^x and the damping coefficient K_{visc}^x. The mass of the maglevtube must be previously measured with a microbalance.

6.1. Experimental calibration

On the experimental setup, the procedure consists in using the rear coils driven by a transient current i (one pulse). The current i is canceled two seconds before t_1. The acquisition of l starts at t_1 when the maglevtube is in ZIR configuration. Figure 15 shows the matching between both experimental and reconstructed ZIR after the parametric identification of the second-order model (17) (done with Matlab identification toolbox). The unknown initial conditions necessary to reconstruct the ZIR in figure 15 are also estimated during the ZIR identification process. The measurement is done with the sensor located on a antivibration pneumatic table and inside a test chamber to reduce air perturbations. The room is mechanically well isolated from the rest of the laboratory on the same floor but is not isolated from the vibrations induced by the bottom floor. Maglevtube natural vibrations before the pulse current are due to the vibrations in the floor which are not correctly filtered by the antivibration table and transmitted to the magnets M_1. These vibrations create a non stationary magnetic field and thus unwanted forces on the small magnets M_2 in levitation generating some small low frequency displacements. These vibrations measured in the signal l are smaller early in the morning or late in the evening. Classical standard deviations for l are given in table 3.

Everybody in the room is completely still during the entire measurement process because foot step impacts on the floor are easily detected by the sensor despite the antivibration table (see figure 16). The maglevtube mass m is measured with a precision balance (Ohaus AR0640 with a readability of 0.1 mg and a repeatability σ_m equal to 0.1 mg). The measured stiffness variations obtained with 10 successive identification trials done in the same conditions give a stan-

	Standard deviation (m)
7:30 am	0.99×10^{-7}
10:00 am	2.02×10^{-7}
3:00 pm	5.03×10^{-7}
7:30 pm	1.72×10^{-7}

Table 3: Standard deviations of l when $F^x = 0$

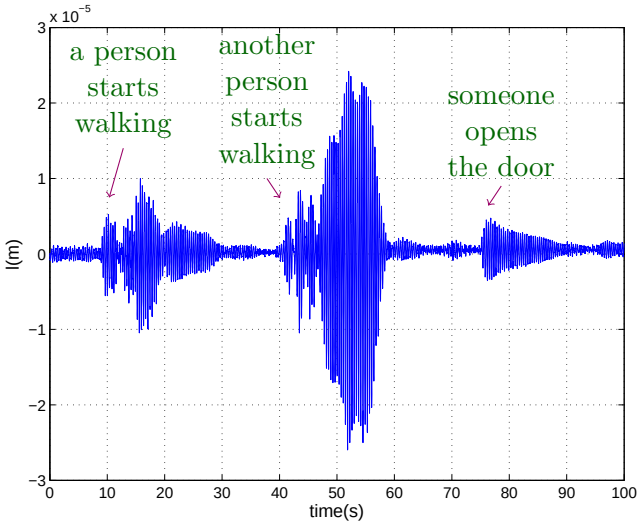

Figure 16: Disturbance of the measured distance l due to step impacts.

dard deviation of 0.0001 N/m (0.5 % of the identified stiffness) on K_m^x. Typical K_m^x values are between 0.01 and 0.03 N/m depending on the maglevtube mass and the magnets M_1 configuration.

6.2. Measurement error analysis in simulation

During calibration, the maglevtube oscillates in a given direction of space and the external force to be measured should not change this direction. The greater the change is in this direction, when the external force is applied, the less correct is the force measurement with the identified stiffness K_m^x. It is possible to have an idea of the measurement error thanks to a simulation approach. The force is computed in steady-state according to equation (15):

$$F^x = K_m^x \, x \tag{22}$$

The measurement of x is l, thus an estimation of F^x is:

$$\hat{F}^x = K_m^x \, l \tag{23}$$

The displacement measurement l is calculated with the simulator presented in section 4. l is corrupted by a gaussian noise with a zero mean and a standard deviation equal to 0.012×10^{-6} meters (the same value as a real STIL SA CL2 confocal chromatic sensor used in the same conditions). The stiffness K_m^x in (23) is given by the ZIR identification done with the simulator. In these conditions, real K_m^x is 0.02892 N/m and identified K_m^x is 0.02859 N/m. When a given external force F^x is applied on the maglevtube, the component x_G and z_G are acquired after the oscillating behavior becomes hidden in the output noise of l (quasi steady-state reached). Note that without external force l, x_G and z_G are considered equal to zero. The evolution of the altitude in quasi steady-state is shown in figure 17. This plot shows that the variation of the maglevtube altitude is not negligible. For $F^x = -30\,\mu$N the variation of z_G reach 24 μm.

Figure 18 shows the ratio $\alpha = \frac{x_G}{l} - 1$ versus F^x. This figure estimates how the measurement of l represents x_G. For a perfect match between the confocal measurent of l and the displacement of the maglevtube along $\vec{x}$, α should be equal to zero.

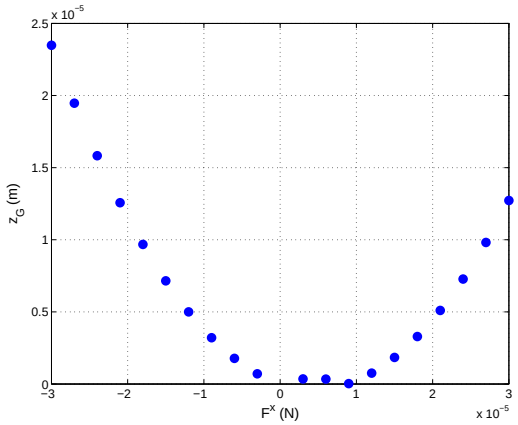

Figure 17: Maglevtube altitude z_G versus F^x in steady-state.

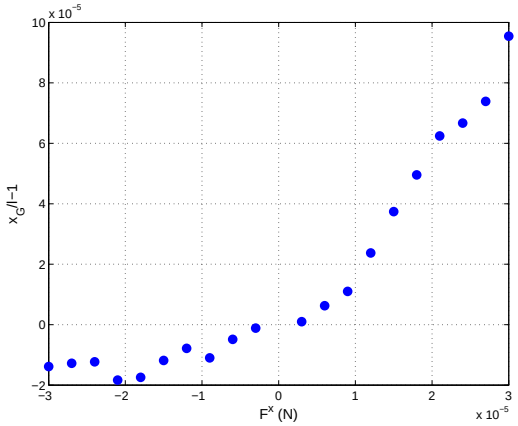

Figure 18: Error between l and x_G using ratio $\alpha = \frac{x_G}{l} - 1$ versus F^x in steady-state.

F^z (% F^x)	relative error (%)
1 %	-0.15
2 %	-0.03
5 %	0.26
10 %	0.55

Table 4: Influence of the applied force direction on the measured force ($\|\vec{F}\| = 1\mu$N).

In these conditions, table 4 gives the typical relative errors when force $\vec{F}$ which is equal to 1 μN (constant modulus) is applied with a vertical component F^z different from zero:

$$\vec{F} \begin{bmatrix} F^x \\ 0 \\ F^z \end{bmatrix} \qquad \|\vec{F}\| = 1\mu\text{N} \tag{24}$$

The evolution of the relative error depends on the combination of rotation and translation behavior of the maglevtube which influences the position of the point I (see figure 10).

In the following, it will be assumed that the maglevtube oscillates horizontally along $\vec{x}$ and thus the calibration is only valid if the external force is applied under assumption (4).

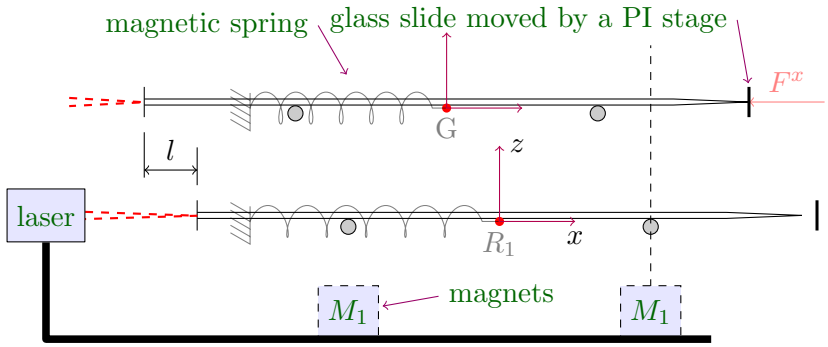

Figure 19: Experimental setup of the maglevtube in contact with a glass slide.

7. Experimental measurement of a micro/nanoforce

After the identification step giving K_m^x, the measured force F^x is estimated using the distance l measured by the CL2 confocal chromatic sensor. This sensor is connected to a Dspace real-time digital signal processor via a RS232 link. Measured data l are sent to the Dspace at $T_s = 100$ Hz. A Simulink model running on the Dspace acquires the data l and estimates the force F^x according to the equation (23) which is only valid in steady-state.

On the experimental setup the force F^x is generated by the contact of a rigid surface as a glass microscope slide on the maglevtube tip (see figure 19). The process consists in moving the glass slide along the $\vec{x}$ axis until it comes into contact with the tip. The motion of the glass slide is provided by three Physik Instrumente motorized translation stages (PI M-122). This whole setup is run under a camera to provide a visualization of the glass slide and the maglevtube tip.

The glass slide is brought into contact with the tip at 5 μm/s. The goal is to measure the pull-off force that is necessary to separate the tip from the slide. The measured force F^x is given in figure 20. The data provided are not filtered. The sequence is composed of four steps:

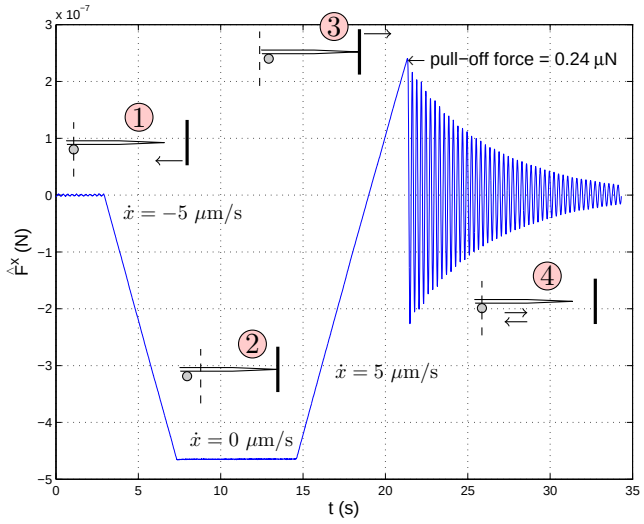

Figure 20: Experimental measurement of nanoforces

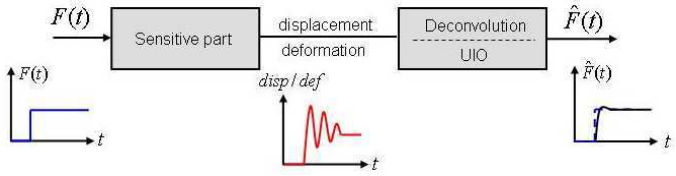

Figure 21: Force estimation using a deconvolution or an unknown input observer of the maglevtube displacement.

① Initial approach ($F^x = 0$)

② Contact between the tip and the slide, loading until F^x reaches -0.46 μN

③ Unloading until $F^x = -0.24$ μN, the contact between the slide and the tip is broken at this level. The measured force corresponds to the pull-off force

④ The slide is removed. The force measured F^x should be equal to zero again in this non-contact configuration. This is not the case because the equation (23) should not be used when the maglevtube is not in a steady-state. In this more complex case, the dynamic of the maglevtube must be taken into account in a deconvolution stage to correctly estimate the force F^x (see figure 21).

The equation (23) is theoretically valid only if $\dot{x}$ and $\ddot{x}$ are equal to zero (steady-state). During steps 1 to 3, $\ddot{x}$ is equal to zero but $\dot{x}$ is either equal to zero or to 5 μm/s (see figure 20). When $\dot{x}$ is different from zero, the equation (23) gives a biased result because the viscous friction force F^x_{visc} is not taken into account (see equation (14)). Nevertheless this bias is completely negligible compared to the measured force because F^x_{visc} is equal to 0.1 nN for the speed $\dot{x}$ considered. In this experiment with non filtered data, the resolution is about 5 nN (peak to peak amplitude noise) on a range of ± 80 μN.

8. Conclusion

This article describes the modeling and some important characteristics of a long range micro-nano force sensor based on a levitating seismic mass. This mass is a ten-centimeter capillary tube stuck on two small magnets and called a maglevtube. Focus has been placed both on the dynamic and the stationary behaviour of the maglevtube using a non linear modeling and a linearized modeling for limited displacements of the seismic mass. Thanks to a specific magnetic spring design, this behaviour is close to a classical spring with a second-order under-damped dynamic and the associated stiffness can be considered as quasi-constant even for long displacements of the maglevtube ($\pm$ 1.5 mm). This stiffness is similar to the stiffness of a thin AFM cantilever and can be easily adjusted. The linearity of the associated force/displacement characteristic in the steady-state has been studied in simulation. Despite the low stiffness, the fact that the stiffness is practically linear even for a long displacement enables force measurement in a range which spreads over the nanonewton scale to one hundred micronewtons, to be possible, when using the same maglevtube and the same confocal sensor. This is very uncommon. The main drawback is the very small bandwidth (a few hertz) due to the macroscopic nature of the seismic mass. Designing or gluing specific tip on the end of the glass tube can also be a complex problem. From a practical point of view, the use of a macroscopic seismic mass makes the mavlevtube easy to handle. Because the maglevtube is very sensitive to any air disturbance, it is necessary to put the sensor inside a closed chamber located on a antivibration table. The calibration process of the sensor is based on a zero input response that makes the complete parametric identification of the linear dynamic model possible. If the maglevtube mass is known, this identification gives the stiffness as well as the viscous friction coefficient. In the steady-state, only the stiffness identification is necessary to estimate the external force applied to the maglevtube. On the contrary, if the dynamic of the maglevtube (speed and acceleration) is not negligible, the force estimation necessitates the knowledge of the complete parametric model and thus the vis-

cous coefficient identification. In this case, the reconstruction of the force is possible using a deconvolution approach or an unknown input observer design. This point is an outlook for this article. The external force should be applied to the maglevtube along the direction corresponding to the calibration process. To be verified, this condition needs the determination of the maglevtube complete attitude (position and orientation). Because this reconstruction is impossible with only a single displacement sensor, simulated results have been presented to give an idea of the force measurement error achieved when the applied force is not correctly aligned with the maglevtube calibrated direction. The last part of the paper consists in the illustration of a real force measurement. The goal is to experimentally determine a pull-off force between a glass tip and a given material. Because of the small dynamic involved in this experiment, we focused the study on the stationary behaviour in steady-state in order to illustrate the force measurement. Experimental data presented are not filtered thanks to the good quality of measurement provided by the CL2 confocal chromatic sensor manufactured by STIL SA.

Acknowlegments

This work is supported by the French National Research Agency under STILμFORCE contract ANR-07-ROBO-0005.

References

[1] M. Sepaniak, P. Datskos, N. Lavrik, and C. Tipple, "Microcantilever transducers: A new approach in sensor technology," *Analytical chemistry*, pp. 568–575, November 2002.

[2] P. Rougeot, S. Régnier, and N. Chaillet, "Forces analysis for micromanipulation," *Proceedings 2005 IEEE international symposium on computational intelligence in robotics and automation, espoo, Finland*, pp. 105–110, june 2005.

[3] M. Girot, M. Boukhalel, and S. Régnier, "Towards a non-destructive in vitro biomechanical characterization," *ASM - IEEE EMBS Conference on Bio-, Micro- and Nanosystems, San Francisco, USA*, janvier 2006.

[4] N. Kato, I. Suzuki, H. Kikuta, and K. Iwata, "Force-balancing microforce sensor with an optical-fiber interferometer," *Review of scientific instruments*, vol. 68, pp. 2475–2478, juin 1997.

[5] F. Arai, A. Kawaji, T. Sugiyama, Y. Onomura, M. Ogawa, T. Fukuda, H. Iwata, and K. Itoigawa, "3d micromanipulation system under microscope," *International symposium on micromechatronics and human science*, pp. 127–134, 1998.

[6] F. Arai, D. Andu, Y. Nonoda, T. Fukuda, H. Iwata, and K. Itoigawa, "Micro endeffector with micro pyramids and integrated piezoresistiveforce sensor," *proc. of int. conf on intelligent robots and systems, IROS 96*, vol. 2, pp. 842–849, 1996.

[7] Y. Sun, W. Kai-Tak, K. Roberts, J. Bischof, and J. Bradley, "Mechanical property characterization of mouse zona pellucida," *IEEE transactions on nanobioscience*, vol. 2, no. 4, pp. 279–285, December 2003.

[8] Y. Sun, N. Fry, D. Potasek, D. Bell, and B. Nelson, "Characterizing fruit fly flight behaviour using a microforce sensor with a new comb-drive con-

figuration," *Journal of microelectromechanical systems*, vol. 14, pp. 4–11, 2005.

[9] W. Li and N. Xi, "Novel micro gripping, probing and sensing devices for single-cell surgery," *Proceedings of the 26th international conference of the IEEE EMBS San Francisco, CA, USA*, pp. 2591–2594, September 2004.

[10] Y. Shengyuan and S. Taher, "Micromachined force sensors for study of cell mechanics," *Review of scientific instruments 76, 044301*, 2005.

[11] Y. Fujii, "Methode for generating and measuring the micro-newton level forces," *Mechanical Systems and Signal Processing*, vol. 20, pp. 1362–1371, 2006.

[12] C. Gosse and V. Croquette, "Magnetic tweezers : Micromanipulation and force measurement at the molecular level," *Biophysical Journal*, 2002.

[13] Z. Dai, S. N.Gorb, and U. Schwarz, "Roughness-dependent friction force of the tarsal claw system in the beetle pachnoda marginata (coleoptera, scarabaeidae)," *The journal of experimental biology*, vol. 205, pp. 2479–2488, 2002.

[14] A. Varenberg, S. Peressadko, S. Gorb, E. Arzt, and S. Mrotzek, "Advanced testing of adhesion and friction with microtribometer," *Review of scientific instruments*, vol. 77, pp. 066 105–1 to 066 105–3, 2006.

[15] "http://www.mstnews.de/downloads/pdf/news-0507.pdf."

[16] Yang and Saif, "Micromachined force sensors for the study of cell mechanics," *Review of Scientific Instruments*, 2008.

[17] K. Kim, X. Liu, Y. Zhang, and Y. Sun, "Nanonewton force-controlled manipulation of biological cells using a monolithic mems microgripper with two-axis force feedback," *Journal of Micromechanics and Microengineering*, 2008.

[18] S. Fahlbush and S. Fatikow, "Micro-force sensing in a micro robotic system," *Proc. IEEE Int. Conf. on Robotics and Automation*, pp. 3435–3440, 2001.

[19] F. Arai, T. Sugiyama, T. Fukuda, H. Iwata, and K. Itoigawa, "Micro tripaxial force sensor for 3d bio-micromanipulation," *In IEEE International Conference on Robotics and Automation (ICRA)*, 1999.

[20] F. Beyeler, A. Neild, S. Oberti, D. J. Belly, Y. Sun, J. Dual, and B. J. Nelson, "Monolithically fabricated microgripper with integrated force sensor for manipulating microobjects and biological cells aligned in ultrasonic field," *Journal of Microelectromechanical Systems*, 2007.

[21] Y. Shen, N. Xi, and W. J. li, "Contact and force control in microassembly," *In IEEE 5th International Symposium on Assembly and Task Planning (ISATP)*, 2003.

[22] F. Beyeler, S. Muntwyler, and B. J. Nelson, "A six-axis mems force-thorque sensor with micro-newton and nano-newtonmeter resolution," *Journal of Microelectromechanical Systems*, 2009.

[23] S. Muntwyler, F. Beyeler, and B. J. Nelson, "Three-axis micro-force sensor with sub-micro-newton measurement uncertainty and tunable force range," *Journal of Micromechanics and Microengineering*, 2010.

[24] S. B. Aksu and J. A. Turner, "Calibration of atomic force microscope cantilevers using piezolevers," *Review of Scientific Instruments*, 2007.

[25] S. Earnshaw, "On the nature of the molecular forces," *Trans. Cambridge phil.Soc.*, vol. 7, pp. 97–112, 1842.

[26] A. Boerdijik, "Technical aspects of levitation," *Philips Resarch Reports*, vol. 11, pp. 45–46, Dec. 1956.

[27] M. Boukallel, E. Piat, and J. Abadie, "Passive diamagnetic levitation : theoretical foundations and application to the design of a micro-nano force

sensor," in *Proc. of the IEEE/RSJ International Conference on Intelligent Robots and Systems, IROS'2003*, 2003, pp. 1062–1067.

[28] M. Boukallel, "Etude, conception et réalisation d'un capteur de micro et nano-forces. application à la mesure d'élasticité des ovocytes," Ph.D. dissertation, Université de Franche Comté, 2003.

[29] J. R. Wertz, *Spacecraft Attitude Determination and Control*. Springer, 1978.

[30] R. S. Gates and J. R. Pratt, "Prototype cantilevers for si-traceable nanonewton force calibration," *Measurement Science and Technology*, vol. 17, no. 10, pp. 2852 – 2860, 2006.

[31] I. Palaci, "Atomic force microscopy studies of nanotribology and nanomechanics," Ph.D. dissertation, Ecole Polytechnique Fédérale de Lausane, 2007.

[32] H. Fujimoto and Y. Fujii, "Measurement of step impulse response of a force transducer," *Measurement Science and Technology*, vol. 14 (1), pp. 65–69, 2003.

[33] Y. Fujii and H. Fujimoto, "Proposal for an impulse response evaluation method for force transducers," *Measurement Science and Technology*, vol. 10 (4), pp. N31–N33, 1999.

[34] Y. Fujii, "Proposal for a step response evaluation method for force transducers," *Measurement Science and Technology*, vol. 14 (10), pp. 1741–1746, 2003.

[35] R. Kumme, "Investigation of the comparison methode for the dynamic calibration of force transducers," *Measurement*, vol. 23, pp. 239–245, 1998.

[36] Y. Park, R. Kumme, and D. Kang, "Dynamic investigation of a binocular six-component force-moment sensor," *Measurement Science and Technology*, vol. 13, pp. 1311–1318, 2002.

[37] Y. Fujii, "A methode for calibrating force transducers against oscillation force," *Measurement Science and Technology*, vol. 14 (8), pp. 1253–1264, 2003.

[38] Y. Park, R. Kumme, and D. Kang, "Dynamic investigation of a three-component force-moment sensor," *Measurement Science and Technology*, vol. 13, pp. 654–659, 2002.